

## DIFFUSE X-RAY EMISSION FROM STAR FORMING GALAXIES

KARTICK C. SARKAR<sup>1,2,\*</sup>, BIMAN B. NATH<sup>1</sup>, PRATEEK SHARMA<sup>2</sup>, YURI SHCHEKINOV<sup>3</sup>

<sup>1</sup> Raman Research Institute, Sadashiva Nagar, Bangalore 560080, India

<sup>2</sup> Joint Astronomy Programme and Dept. of Physics, Indian Institute of Science, Bangalore, 560012, India and

<sup>3</sup> P. N. Lebedev Physical Institute, 53 Leninskiy Prospekt, 119991, Moscow, Russia

*Draft version December 3, 2024*

### ABSTRACT

We study the diffuse X-ray luminosity ( $L_X$ ) of star forming galaxies using 2-D axisymmetric hydrodynamical simulations and analytical considerations of supernovae (SNe) driven galactic outflows. We find that the mass loading of the outflows, a crucial parameter for determining the X-ray luminosity, is constrained by the availability of gas in the central star forming region, and a competition between cooling and expansion. We show that the allowed range of the mass loading factor can explain the observed scaling of  $L_X$  with star formation rate (SFR) as  $L_X \propto \text{SFR}^2$  for  $\text{SFR} \gtrsim 1 \text{ M}_\odot \text{ yr}^{-1}$ , and a flatter relation at low SFRs. We also show that the emission from the hot circumgalactic medium (CGM) in the halo of massive galaxies can explain the sub-linear behaviour of the  $L_X$ –SFR relation as well as a large scatter in the diffuse X-ray emission for low SFRs ( $\lesssim \text{few M}_\odot \text{ yr}^{-1}$ ). Our results point out that galaxies with small SFRs and large diffuse X-ray luminosities are excellent candidates for detection of the elusive CGM.

*Subject headings:* galaxies: general, starburst, halo – X-rays: galaxies – ISM: jets and outflows

### 1. INTRODUCTION

Understanding the feedback mechanisms in galaxies is crucial in order to explain the evolution of galaxies (Larson 1974; Dekel & Silk 1986; Sharma & Nath 2013) and enrichment of the intergalactic medium (IGM) (Tegmark & Silk 1993; Nath & Trentham 1997). It has been observed (Strickland et al. 2002; Strickland & Heckman 2007) and noticed in numerical simulations (Hopkins et al. 2012; Sarkar et al. 2015, hereafter S15) that a significant fraction ( $\sim 0.3 - 0.5$ ) of the input mechanical energy is stored in a hot ( $T \gtrsim 10^6 \text{ K}$ ), X-ray emitting gas. Therefore, it is necessary to decipher the origin of diffuse X-ray emission from star forming galaxies to understand the feedback mechanisms.

In the case of stellar feedback processes producing a gaseous outflow, the hot gas can form in (i) the central region where star formation occurs, (ii) the free wind, (iii) the interaction zone between the wind and halo gas surrounding the galaxy, and (iv) the interaction region of wind and dense clouds (Suchkov et al. 1994, 1996; Strickland & Stevens 2000; Cooper et al. 2008, 2009; Thompson et al. 2015). In addition, there is a non-negligible contribution from the hot halo gas surrounding the galaxies. For well-resolved galaxies, this basic scenario can be used to investigate the kinematic properties of the wind. For example, using X-ray observations, Strickland & Heckman (2007) found that the velocity of the outflow in the central region ( $\sim 100 \text{ pc}$ ) of M82 can be as large as  $\sim 10^3 \text{ km s}^{-1}$  and the mass outflow rate in the hot phase is  $\sim 1/3$  of the SFR in that galaxy.

However, some aspects of the diffuse X-ray emission remain puzzling. Using 2D axisymmetric simulations for a galaxy with  $\text{SFR} \sim 1 \text{ M}_\odot \text{ yr}^{-1}$ , Suchkov et al. (1994) found that the shocked halo emission dominates over the emission from the central part. In contrast, using a full

3D simulation of M82 ( $\text{SFR} \sim 10 \text{ M}_\odot \text{ yr}^{-1}$ ) Cooper et al. (2008) showed that most of the emission comes from the central region and free wind rather than halo. Cooper et al. (2008, 2009) also noticed that a part of the emission comes from the interaction of clouds and the high velocity wind. However, a quantitative description of this emission is unavailable.

Another problem involves the scaling relation between the diffuse X-ray luminosity (not associated with point sources directly or indirectly) and the SFR. A thermally driven wind model (Chevalier & Clegg 1985, hereafter, CC85)<sup>1</sup> suggests that the hot gas density at the central region of galactic wind is  $\propto \text{SFR}$ , and therefore, the X-ray luminosity  $\propto \text{SFR}^2$ . The temperature of the gas related to the wind or shocked halo is  $\lesssim 2 \times 10^7 \text{ K}$  which emits mostly in the soft band (0.5–2.0 keV). A recent observational study of diffuse X-ray emission, however, suggests that the soft X-ray luminosity,  $L_X \propto \text{SFR}$  (Mineo et al. 2012, hereafter, M12), though other scalings cannot be ruled out. Zhang et al. 2014 and Bustard et al. 2015 attempted to reconcile the observations with the expected scaling by adjusting parameters such as the mass loading factor (MLF; mass outflow rate/SFR =  $\beta$ ) and the thermalisation efficiency ( $\alpha$ ). They suggested that an inverse dependence of  $\beta$  on SFR in order to explain the observed  $L_X$ –SFR relation. However, the physical origin for such an inverse relation remains unexplained.

Yet another problem is that galaxies with low SFR ( $\leq \text{few M}_\odot \text{ yr}^{-1}$ ) show a flatter  $L_X$ –SFR relation with large scatter in the diffuse X-ray luminosity (Wang et al. 2015, hereafter, W15), implying that other factors beyond stellar feedback contribute significantly to X-ray emission.

<sup>1</sup> Note that, the CC85 model with a smooth thermalised wind is only applicable for SFRs larger than a critical value ( $\approx 0.1 \text{ M}_\odot \text{ yr}^{-1}$ ) (Sharma et al. 2014). Therefore, CC85 is a good approximation in the range of SFRs of our interest.

\*kcsarkar@rri.res.in

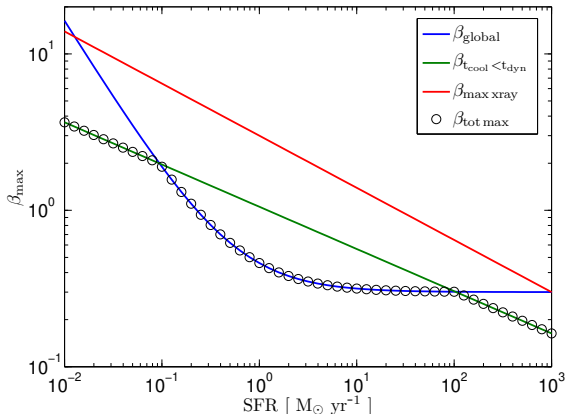


FIG. 1.— Threshold values of MLF ( $\beta$ ) as a function of SFR from various considerations: the availability of gas mass (blue); cooling time (green); and X-ray luminosity in the central region (red). The maximum allowed  $\beta$  is shown by circles. Parameters used here are  $R = 200$  pc,  $n_{\text{ISM}} = 10 \text{ cm}^{-3}$ ,  $\Delta t = 30$  Myr,  $\alpha = 0.3$  and metallicity =  $Z_{\odot}$ .

In this letter, we constrain the mass loading factor based on the amount of interstellar medium (ISM) mass available and by the requirement that the cooling time be longer than the outflow expansion time. Using this, we show that at large SFRs the X-ray luminosity ( $L_X$ ) indeed scales as  $\text{SFR}^2$ , but at smaller SFRs the X-ray emission from the circumgalactic medium (CGM; which is insensitive to SFR) starts to dominate. This behaviour can lead to the observed  $L_X \propto \text{SFR}$  if one fits a single power law to observations.

The paper is organised as follows. We start with describing constraints on MLF in section 2. Brief simulation details are given in section 3. In section 4, we present the results from our analytical considerations and simulations and show the consistency of our model with the data. Finally, we discuss the implications of our results in section 5.

## 2. MASS LOADING OF OUTFLOWS

Consider galaxies with outflows driven by thermal feedback from star formation, which we model as a thermal wind within a central region of size  $R$  (following CC85). The energy and mass injection in the central zone is parametrised by  $\dot{M}$  and  $\dot{E}$ , which are respectively the mass deposition rate and the energy deposition rate, and are given by  $\dot{M} = \beta \text{SFR}$  and  $\dot{E} = 5 \times 10^{15} \alpha \text{SFR}$  (assuming a Kroupa/Chabrier mass function, and an efficiency  $\alpha \approx 0.3$  for energy deposition; here  $\dot{E}$ ,  $\dot{M}$  and SFR are in CGS units).

The X-ray luminosity of a galactic wind sensitively depends on the MLF,  $\beta$  (Zhang et al. (2014)). MLF is governed by following considerations: (a) Stellar evolution models suggest that stellar winds and supernova ejecta (without entrainment from the surrounding ISM) contribute to  $\beta_0 \approx 0.3$  (Leitherer et al. 1999), (b) the outflowing gas entrains mass from the surrounding ISM. However, the entrained mass (due to conduction and KH instabilities) cannot be larger than the total ISM mass  $M_g (= 4\pi\mu m_p n_{\text{ISM}} R^3/3)$  available within the central starburst region of radius  $R$ . Therefore, an upper limit of

MLF is given by

$$\beta_{\text{global}} = \beta_0 + \frac{M_g/\Delta t}{\text{SFR}} = 0.3 + 0.06 \times \frac{n_{\text{ISM}} R_{100\text{pc}}^3}{\text{SFR}_{\text{M}_{\odot} \text{ yr}^{-1}} \Delta t_{\text{Myr}}}, \quad (1)$$

where,  $n_{\text{ISM}}$  is the ambient ISM number density,  $\Delta t$  is the age of the starburst. (c) A further constraint arises from the cooling time of this central gas to be longer than the expansion time, otherwise most mass will condensate radiatively and drop out of the outflow (see equation 10 of Thompson et al. 2015; for a wind opening angle of  $60^\circ$ ). (d) A related constraint is that for the total X-ray luminosity of the central region ( $\approx 4\pi n_c^2 \Lambda(T_c) R^3/3$ ; where,  $n_c = 0.3 \dot{M}^{3/2} \dot{E}^{-1/2} R^{-2} / \mu m_p$  is the central ISM number density;  $\mu = 0.6$ , is the mean molecular weight;  $\Lambda$  is the cooling function ( $\text{erg s}^{-1} \text{cm}^{-3}$ );  $T_c = 1.4 \times 10^7 \alpha / \beta$ , is the central temperature (see CC85)) should be smaller than the energy deposition rate ( $\dot{E}$ ). This gives an upper limit on MLF, namely,

$$\beta_{\text{max xray}} = \left( \frac{13.5 \alpha_{0.3}^2 R_{100\text{pc}}}{\text{SFR}_{\text{M}_{\odot} \text{ yr}^{-1}} \Lambda_{-23}(T, Z)} \right)^{1/3}, \quad (2)$$

where,  $\Lambda_{-23}(T, Z)$  is the emission function at a particular X-ray energy band (in units of  $10^{-23} \text{ erg s}^{-1} \text{cm}^{-3}$ ), temperature ( $T$ ) and metallicity ( $Z$ ).

In the case of high  $\beta$ , the outflowing gas has a large ram pressure ( $\propto \dot{M}^{1/2} \dot{E}^{1/2} \propto \beta^{1/2}$ ) on the surrounding gas, and is likely to entrain more gas. It is therefore reasonable to assume that  $\beta$  is likely to attain the maximum allowed value under the above considerations (b,c,d in previous paragraph). Figure 1 shows various threshold values of  $\beta$  as a function of SFR. Open circles show the maximum values of  $\beta$  allowed by these considerations.

## 3. SIMULATION DETAILS

We perform 2-D axisymmetric hydrodynamic simulations using PLUTO (Mignone et al. 2007). We simulate only one quadrant of a MW type galaxy (total mass  $M_{\text{vir}} = 10^{12} M_{\odot}$ ). The initial condition for the galaxy is in dynamical equilibrium with of a warm, rotating disc ( $T \sim 4 \times 10^4$  K; with Solar metallicity) and a hot gaseous halo ( $T = 3 \times 10^6$  K; with 0.1 Solar metallicity) surrounding the galaxy. We vary SFR for the same disc/halo properties. The disc gas is not allowed to cool if it is not shocked/perturbed; i.e., unless  $\sqrt{v_r^2 + v_\theta^2} \geq 20 \text{ km s}^{-1}$ . Other details of the model can be found in S15.

The SNe energy is deposited continuously in form of thermal energy in a spherical region of radius  $R$  at the centre of the galaxy. In reality, most of the SNe occurs in a low density medium created by the previous SNe explosions and stellar winds. To mimic this, we create an artificially low density medium ( $10^{-2} m_p \text{ cm}^{-3}$ ) at  $t = 0$  for  $r \leq R$  (in local pressure equilibrium with the region outside) and then deposit the SNe energy and mass (with  $Z_{\odot}$ ) inside it. This also prevents artificial cooling losses due to lack of sufficient numerical resolution. For estimating the X-ray emission function ( $\Lambda_X(T, Z)$ ), we use MEKAL model at 0.2 and 1.0  $Z_{\odot}$  and linearly interpolate for all other metallicities (from 0.1 to 1.0  $Z_{\odot}$ ).

## 4. RESULTS

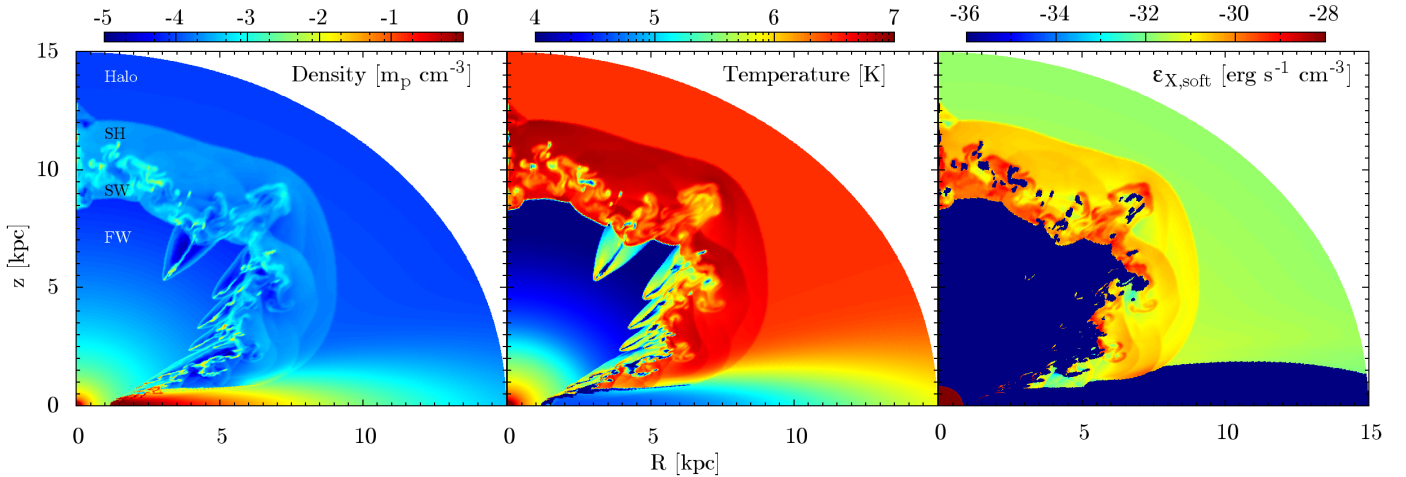


FIG. 2.— Snapshots of density (left panel), temperature (middle panel) and soft X-ray (0.5-2.0 keV) emissivity (right panel) contours at  $t = 20$  Myr for  $\text{SFR} = 5 M_\odot \text{ yr}^{-1}$  and central halo density  $\rho_{h0} = 3 \times 10^{-4} m_p \text{ cm}^{-3}$  with total grid points = 512<sup>2</sup>. The labels in the left panel are as follows: FW- Free Wind, SW- Shocked Wind and SH- Shocked Halo. Note that we have used colourbar between  $10^{-36}$  and  $10^{-28} \text{ erg s}^{-1} \text{ cm}^{-3}$  (right panel) but the core emissivity is  $\sim 10^{-21} \text{ erg s}^{-1}$ .

Figure 2 shows snapshots of density, temperature and soft X-ray emissivity for  $\text{SFR} = 5 M_\odot \text{ yr}^{-1}$  and background halo density  $\rho_{h0} = 3 \times 10^{-4} m_p \text{ cm}^{-3}$  at  $t = 20$  Myr. It shows a typical structure containing free wind, termination shock, shocked wind, shocked halo and unshocked halo as labelled in the left panel (Weaver et al. 1977). The soft X-ray (0.5-2.0 keV) emissivity (right-most panel) shows the origin of X-ray emission in a typical galactic wind. It shows that the X-ray emission comes predominantly from the central region, followed by shocked wind, shocked halo and halo region.

We find that the luminosity of the central region becomes constant after  $t \gtrsim 2$  Myr. Though the contribution of the outer parts (consisting of the shocked wind, shocked halo and the CGM) increases with time because of the increased volume of the shocked halo gas and continuous energy pumping from the wind, the X-ray luminosity from the central injection region and the CGM dominates. Here we present analytic scalings of these components.

Following CC85, the central luminosity (for  $r \leq R$ ) can be estimated in the case of a uniform density ( $\rho_c = \mu m_p n_c$ ) central region (of volume  $4\pi R^3/3$ ) as  $L_{X,C} = 1.3 \times 10^{40} \alpha^{-1} \beta^3 \text{SFR}^2 R_{100\text{pc}}^{-1} \Lambda_{-23}(T, Z) \text{ erg s}^{-1}$ . However this is an overestimate since the density in the central region is not quite uniform. Results from our simulations are well fit by,

$$\frac{L_{X,C}}{\text{erg s}^{-1}} \approx 3 \times 10^{39} \alpha^{-1} \beta^3 \text{SFR}^2 R_{100\text{pc}}^{-1} \Lambda_{-23}(T, Z). \quad (3)$$

The next important contribution towards X-ray emission comes from the CGM which contains a significant fraction of the missing baryonic mass, as seen in X-ray (Anderson & Bregman 2011; Bogdan et al. 2012; Dai et al. 2012) and absorption studies (Bordoloi et al. 2014; Borthakur et al. 2015).

The CGM density profile can be approximated as  $n_0 (1 + r/r_c)^{-3/4}$ , with a core radius  $r_c$  ( $\approx 3$  kpc) and central density  $n_0$  (see Figure 1 of S15). While this is clearly an approximation, the density values are not that different from estimates in the literature (e.g., Sharma et al. 2012; Fang et al. 2013; Gatto et al. 2013). If the

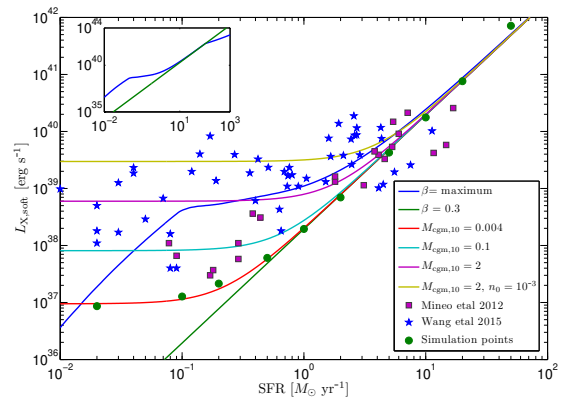


FIG. 3.— Comparison of the soft X-ray luminosities and observed data (magenta squares for M12 and blue asterisk for W15) for various models. The green and blue lines show  $L_{X,C}$  for  $\beta = 0.3$  and  $\beta_{\text{max}}$  for  $R = 200$  pc. The inset shows that  $L_X \propto \text{SFR}$  at larger SFRs ( $\gtrsim 100 M_\odot \text{ yr}^{-1}$ ) where cooling threshold becomes more important than mass loading (see Fig. 1). The red, cyan and magenta lines show  $L_X (= L_{X,C}(\beta = 0.3) + L_{X,CGM})$  for  $n_{0,-3} = 0.3$ , whereas, the golden line shows  $L_X$  for  $n_{0,-3} = 1$ . Notice that, high values of  $L_X$  ( $\sim 10^{40} \text{ erg s}^{-1}$ ) for low SFR galaxies can be obtained for moderate values of  $M_{CGM}$  but using a higher value of  $n_{0,-3}$  (also see eq. 4).

CGM gas is spread over a length scale  $r/r_c = x \gg 1$ , then the X-ray luminosity can be expressed in terms of  $M_{CGM} (= 10^{10} M_{CGM,10} M_\odot)$ , the total CGM gas mass (we express the dependence of  $L_{X,CGM}$  on the extent of the CGM in terms of  $M_{CGM}$ ), as  $L_{X,CGM} \approx 5.4 \times 10^{40} n_{0,-3}^{4/3} r_{c,3} \Lambda_{-23} M_{CGM,10}^{2/3} \text{ erg s}^{-1}$ , where  $n_0 = 10^{-3} n_{0,-3} \text{ cm}^{-3}$  and  $r_c = 3 r_{c,3} \text{ kpc}$ . However, our simulation results show that the actual luminosity from CGM is somewhat less than this, because of the approximation ( $x \gg 1$ ) used in arriving at it, and is better represented by,

$$\frac{L_{X,CGM}}{\text{erg s}^{-1}} \approx 8.6 \times 10^{39} n_{0,-3}^{4/3} r_{c,3} \Lambda_{-23}(T, Z) M_{CGM,10}^{2/3}. \quad (4)$$

Next we compare the X-ray luminosity from our simulations (and scaled according to Eqs 3 and 4 for different

CC85 and CGM properties) with the observed data. Figure 3 shows the  $L_X$ -SFR relation from our models. The green and blue lines show  $L_{X,C}$  for the cases of  $\beta = 0.3$  and the maximum  $\beta$  (circles in Figure 1), respectively. We find that the data from M12, shown in red squares, are explained by  $L_{X,C}$  for the range of  $0.3 \leq \beta \leq \beta_{max}$ , where  $\beta_{max}$  is determined by the available ISM mass and the radiative cooling time, as discussed in section 2, whereas, a higher  $\beta$  for smaller SFRs due to the ISM mass loading makes the relation shallower at smaller SFRs. The data, which have hitherto been fit with a linear scaling between  $L_X$  and SFR, actually belong to two different regimes: a quadratic scaling at large SFRs and a flattening at smaller SFRs. In fact, the constraint of MLF from available ISM mass predicts  $\beta \propto \text{SFR}^{-2/3}$  from 0.1 to a few  $M_\odot \text{ yr}^{-1}$  (Figure 1), which when put in eqn 3 makes  $L_X$  independent of SFR. Note that the ISM mass availability constraint, which we highlight for the first time, is the most stringent for SFRs of interest.

The different lines that flatten towards the lowest SFRs in Figure 3 show the total luminosity (for  $\beta = 0.3$ ) after adding the contribution from CGM with different masses and densities for  $T = 3 \times 10^6 \text{ K}$  and  $Z = 0.1Z_\odot$ . We find that these curves can reasonably explain the data from W15 (shown with the blue stars in Figure 3). The X-ray luminosity in data flattens out at low SFRs because of the contribution from the CGM. W15 also find a dependence of  $L_X$  on stellar mass; namely,  $L_X/L_K \propto (\text{SFR}/M_\star)^{0.3}$  (which is equivalent to  $L_X/\text{SFR} \propto [M_\star/\text{SFR}]^{0.7}$  assuming  $L_K \propto M_\star$ ), where  $L_K$  and  $M_\star$  are K-band luminosity and stellar mass of the galaxies, respectively. The stellar/halo mass dependence can naturally come from the CGM, which is more massive for larger galaxies (see Eq. 4). In fact, the relations above indicate a ‘fundamental plane’ in  $L_X$ ,  $M_\star$  and SFR space, i.e.  $L_X \propto M_\star^{0.7} \text{SFR}^{0.3}$  (for  $\text{SFR} \lesssim \text{few } M_\odot \text{ yr}^{-1}$ ), the existence of which can be tested with future observations.

Since the CGM mass is not yet reliably measured from observations, we can study the relation of  $L_X$  with the expected scaling of CGM mass with stellar/halo mass. Recent observations suggest that about half of the missing baryons is in the form of cold clumps, and the rest could be warm-hot CGM gas (Werk et al. 2014). Since stellar mass comprises about a third, the mass of the warm-hot component of CGM gas can be comparable to  $M_\star$ .

Assuming that the CGM gas mass is equal to the total stellar mass, in Figure 4 we show the relation between  $L_X/\text{SFR}$  and  $M_\star/\text{SFR}$ , where  $M_\star$  is the total stellar mass. The data from W15 are shown along with the curves for different values of  $M_{CGM}(=M_\star)$ . The highest SFR systems lie to left in this plot. The lines with different stellar/CGM masses look reasonably consistent with the data. The observed scaling of  $L_X/\text{SFR} \propto (M_\star/\text{SFR})^{0.6}$  can be easily explained by the scaling of  $L_{X,CGM} \propto M_{CGM}^{2/3}$  (eqn 4), for the CGM X-ray emission, which dominates in the low SFR (right portion of Figure 4). We also notice that the curves in Fig 4 show a negative slope for high SFR galaxies (on the left), which is consistent with the observed trend for high SFR galaxies in W15.

## 5. DISCUSSION

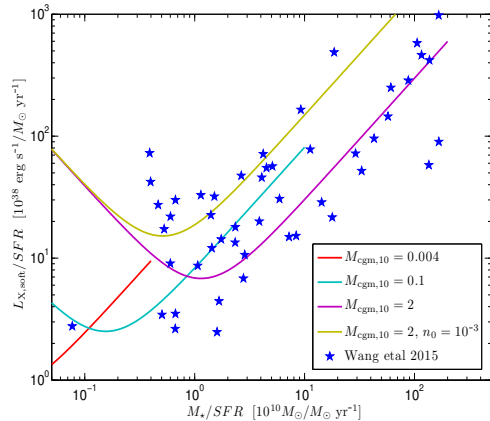


FIG. 4.— Data from W15 along with curves for total diffuse X-ray luminosities for different values of  $M_{CGM}$ . These correspond to the same models as in Figure 3 but normalised to  $M_{CGM} = M_\star$ .

Our key result is that the diffuse X-ray emission from star-forming galaxies can be understood in terms of contributions from the central thermalised wind (extending over  $\sim 100 \text{ pc}$ ) and the extended CGM. For higher SFRs  $L_X \propto \text{SFR}^2$ , whereas, the CGM contribution dominates for  $\text{SFR} \lesssim 1 M_\odot \text{ yr}^{-1}$  and accounts for the flattening of the  $L_X$ -SFR relation at low SFRs. Our model also predicts that the relation can be even flatter with a large scatter, depending on the halo properties. Since the CGM mass is expected to increase with the stellar/halo mass, at smaller SFRs a higher  $L_X$  can result from the CGM contribution. In fact, the galaxies with low SFRs but high  $L_X$  are likely to contain a large amount of CGM gas at temperatures of a few million degrees K, and are good candidates for spiral galaxies with a detectable X-ray emitting CGM (few such systems are reported by Anderson & Bregman 2011; Bogdan et al. 2012).

The X-ray luminosity from the CGM (eqn 4) depends on the CGM gas mass, density and temperature. We find that for the typical range in temperature (as found in, say, W15) of  $2-8 \times 10^6 \text{ K}$ , the  $L_{X,CGM}$  varies between  $3 \times 10^{38} - 2.4 \times 10^{40} \text{ erg s}^{-1}$ , for  $M_{CGM} = 10^{10} M_\odot$ . This spread arises from (a) the difference in emissivity with temperature and (b) the density profile of CGM gas at different temperatures. Figure 3 shows that this spread in X-ray luminosity from the CGM gas can explain the data. We should however keep in mind that the spread in the data Figure 4 can partly arise from the spread in the relation between SFR and galaxy dynamical mass, which is likely related to  $M_\star$  (Karachentsev & Kaisina 2013). We also note that the central SFR used in our models is an underestimation of a disc-wide SFR. This can also be responsible for the spread in the observed data.

It is generally believed that the CGM around low mass galaxies ( $M_\star \lesssim \text{few } \times 10^9 M_\odot$ ) would have a low virial temperature (few  $\times 10^5 \text{ K}$ ), which would make the CGM vulnerable to radiative cooling as the cooling time would become less than the dynamical time of the galaxy (Singh et al. 2015). However, hot CGM around low mass galaxies can be formed from the hot and low density material ejected from disc supernovae which does not have sufficient energy to escape the galactic potential but have a long cooling time. This rejuvenated halo around low

mass galaxies may give rise to the X-rays seen in low mass galaxies (which are also low SFR galaxies, in the presented data). The spread in  $L_X$ -SFR relation at the low SFR end can be partly due to the ill-understood, complex thermodynamic state of such low speed outflows.

Though observations of the *total* X-ray emission (0.5-8.0 keV) (Mineo et al. 2014) show a linear relation, it is, however, supposed to be contaminated by high mass X-ray binaries (HMXB) (Grimm et al. 2003) and should best be considered as an indicator to the SFR (since, number of HMXBs  $\propto$  SFR) rather than diffuse X-ray related to the galactic wind.

We also note that the linear relation of X-ray luminosity from the shocked wind and halo as observed in highly inclined galaxies by Strickland et al. (2004); Tüllmann

et al. (2006); Li & Wang (2013) have to be studied separately as the soft X-ray emission from the central part of these galaxies is heavily absorbed by the galactic disc and does not represent the total emission. We will address these issues in detail in a future paper.

#### ACKNOWLEDGEMENTS

We are indebted to Daniel Q. Wang for sharing data with us and for his useful comments. We also thank Nazma Islam for useful discussions. This work is partly supported by the DST-India grant no. Sr/S2/HEP-048/2012 and an India-Israel joint research grant (6-10/2014[IC]). YS acknowledges support from RFBR through 15-02-08293 and 15-52-45114, and partial support from the Grant of the President of RF for the Leading Scientific Schools NSh-4235.2014.2 .

#### REFERENCES

- Anderson M. E., Bregman J. N., 2011, *ApJ*, 737, 22  
 Bustard C., Zweibel E. G., D’Ongia E., 2015, *Arxiv*: 1509.07130  
 Bogdán Á., et al. , 2013, *ApJ*, 772, 97B  
 Bordoloi R., et al. , 2014, *ApJ*, 796, 136B  
 Borthaku S., et al. , 2015, *ApJ*, 813, 46B  
 Chevalier R. A., Clegg A. W., 1985, *Nature*, 317, 44  
 Cooper J. L., Bicknell G. V., Sutherland R. S., 2008, *ApJ*, 674, 157  
 Cooper J. L., Bicknell G. V., Sutherland R. S., Bland-Hawthorn J., 2009, *ApJ*, 703, 330  
 Dai X., Anderson M. E., Bregman J. N., Miller J. M., 2012, *ApJ*, 755, 107  
 Dekel A. & Silk J., 1986, *ApJ*, 303, 39  
 Fang T., Bullock J., Boylan-Kolchin M., 2013, *ApJ*, 762, 20  
 Gatto A., Fraternali F., Read J. I., Marinacci E., Lux H., Walch S., 2013, *MNRAS*, 433, 2749  
 Grimm H.-J., Gilfanov M., Sunyaev R., 2003, *MNRAS*, 339, 793  
 Hopkins P. F., Quataert E., Murray N., 2012, *MNRAS*, 421, 3522  
 Karachentsev I. D., Kaisina E. I., 2013, *AJ*, 146, 46  
 Larson R., 1974, *MNRAS*, 169, 229  
 Leitherer C. et al. , 1999, *ApJSS*, 123, 3  
 Li J., Wang Q. D., 2013, *MNRAS*, 428, 2085  
 Mignone, A., Bodo, G., Massaglia, S., Matsakos, T., Tesileanu, O., Zanni, C., Ferrari, A., 2007, *ApJSS*, 170, 228  
 Mineo S., Gilfanov M., Sunyaev R., 2012, *MNRAS*, 426, 1870  
 Mineo S., Gilfanov M., Lehmer B. D., Morrison G. E., Sunyaev R., 2014, *MNRAS*, 437, 1698  
 Nath B. B., Trentham N., 1997, *MNRAS*, 291, 505  
 Sarkar K. C., Nath B. B., Sharma P., Shchekinov Y., 2015, *MNRAS*, 448, 328  
 Sharma M. & Nath B. B., 2013, *ApJ*, 763, 17  
 Sharma P., McCourt M., Parrish I. J., Quataert E., 2012, *MNRAS*, 427, 1219  
 Sharma P., Roy A., Nath B. B., Shchekinov Y. , 2014, *MNRAS*, 443, 3463  
 Singh, P. Nath B. B., Majumdar, S., Silk, J. 2015, *MNRAS*, 448, 2384  
 Strickland D. K. & Stevens I. R., 2000, *MNRAS*, 314, 511  
 Strickland D. K., Heckman T. M., Weaver K. A., Hoopes C. G., Dahlem M., 2002, *ApJ*, 568, 689  
 Strickland D. K., Heckman T. M., Colbert J. M., Hoopes C. G., Weaver K. A., 2004, *ApJ*, 606, 829  
 Strickland D. K., Heckman T. M., 2007, *ApJ*, 658, 258  
 Suchkov A. A., Balsara D. S., Heckman T. M., Leitherer C., 1994, *ApJ*, 430, 511  
 Suchkov A. A., Berman V. G., Heckman T. M., Balsara D. S., 1996, *ApJ*, 463, 528  
 Tegmark M., Silk J., 1993, *ApJ*, 417, 54  
 Thompson T. A., Quataert E., Zhang D., Weinberg D. H., 2015, *arXiv*: 1507.04362  
 Tüllmann R., Breitschwerdt D., Rossa J., Pietsch W., Dettmar R.-J., 2006, *A&A*, 457, 779  
 Wang Q. D., Li J., Jiang X., Fang T., 2015, *arXiv*: 1512.02655  
 Weaver R., McCray R., Castor J., Shapiro P., Moore R., 1977, *ApJ*, 218, 377  
 Werk J. K., et al. , 2014, *ApJ*, 792, 8  
 Zhang D., Thompson T. A., Murray N., Quataert E., 2014, *ApJ*, 784, 93